RESEARCH ARTICLE

Investigation of the applicability of conditioned particle image velocimetry under conditions close to lean blow-off

Xiaoyang Wang[1] · Kunpeng Liu[1] · Chen Fu[1] · Juan Yu[1] · Yi Gao[1]

Abstract

In recent years, conditioned particle image velocimetry (CPIV) has attracted much attention for flame front extraction. It is an economical and straightforward technique because the flame front can be obtained simply from Mie-scattering images. In the current work, Mie-scattering and hydroxyl planar laser-induced fluorescence (OH-PLIF) measurements were taken simultaneously to study the applicability of CPIV under conditions with varying equivalence ratios, and the reliable working range of the CPIV method and the source of bias were clarified quantitatively. The premixed dimethyl ether (DME)/air flames stabilized on a two-dimensional bluff body were tested. It is found that the accuracy of the CPIV method worsens as the equivalence ratio decreases. The bias of CPIV is supposed to be related to the flame structure and aerodynamics. The extraction deviation in the upstream region for the stable flames is more significant than that in the downstream area due to the intensified interaction between the shear layer and flame near the bluff body. However, for the flames approaching the lean blow-off (LBO), the bias in the upstream part is smaller than that in the downstream area, which is related to the "back-support" of the hot recirculation zone (RZ). In addition, the difference between the results obtained by CPIV and OH-PLIF is usually the preheat layer of flame and concave-wrinkled location of OH-PLIF filled with CH_2O radicals, especially under conditions close to the LBO, which can be used to estimate the spatial distribution of CH_2O.

Graphical Abstract
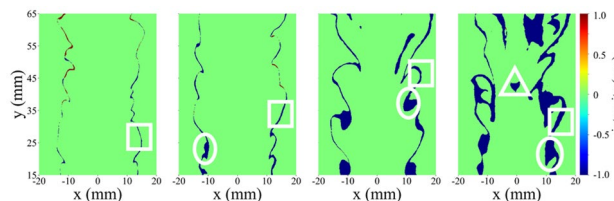
1 Introduction

Turbulent premixed combustion is the mode of operation in industrial applications, such as aero-engines and gas turbines. A deeper understanding of turbulent combustion will help to improve combustion efficiency and stability. It is well established that most of the premixed turbulent flames are composed of wrinkled "flamelets" (Driscoll et al. 2020); thus, the flame can be considered as an ensemble of laminar stretched "flamelets" when the thickness of the chemical reaction layer is smaller than the scale of Kolmogorov eddies (Peters 2000). The thin chemical reaction layer of premixed turbulent flame, known as the flame front, can be used to calculate many critical parameters, such as the flame surface density and flame brush thickness, and the turbulent burning velocity calculation highly depends on these parameters (Driscoll 2008). Thus, the extraction of the flame front is necessary for advanced chemical dynamic calculations and accurate predictions using numerical simulations at a lower cost.

There are several methods to obtain the flame front. The OH radical is a long-lived species during combustion and appears at the flame front and in burnt areas (Nguyen and

✉ Yi Gao
gaoyisjtu@sjtu.edu.cn

1 Shanghai Jiao Tong University, Shanghai 200240, People's Republic of China

Paul 1996). Therefore, the contour of the OH-PLIF signal can be extracted and generally regarded as the approximation of the flame front (Ayoolan et al. 2006; Barlow et al. 2009; Hartung et al. 2009, 2008; Hassel and Linow 2000; Shimura et al. 2011). Additionally, the flame front can also be acquired by employing the Rayleigh thermometry (Knaus et al. 2005), CH-PLIF technique (Tanahashi et al. 2005), and the method of detecting the disappearance of oil droplets within the flame front (Knaus et al. 2002), and so on. Among them, the conditioned particle image velocimetry (CPIV) method has attracted great interest from researchers in recent years (Pfadler et al. 2007). A sharp particle density gradient exists in Mie-scattering images due to the temperature change between the unburnt and burnt zones. Thus, the flame front of a turbulent premixed flame can be deduced from the dense and sparse particle density boundary. Furthermore, the flow field can be obtained simultaneously using the dual Mie-scattering images of the PIV technique without additional expensive and complex devices. Consequently, the CPIV method is widely used in premixed bluff-body flames (Biswas et al. 2013; Chaparro and Cetegen 2006; Geikie et al. 2017; Morales et al. 2021, 2020; Rising et al. 2021; Tuttle et al. 2013), swirling flames (Marshall et al. 2017; Ranjan et al. 2019), V-shaped flames (Pfadler et al. 2009), and Bunsen flames (Pfadler et al. 2008; Tyagi and O'Connor 2020), etc., for the extraction of the flame front.

Recently, the CPIV method has been applied in the premixed flames approaching the lean blow-off (LBO) (Biswas et al. 2013; Chaparro and Cetegen 2006; Morales et al. 2020, Tuttle et al. 2013). Tuttle et al. calculated the local aerodynamic strain rates and curvature using CPIV and investigated the LBO behavior of asymmetrically fueled bluff-body stabilized flames (Tuttle et al. 2013). Biswas et al. utilized the CPIV method to determine the strain rate variations at different phases of the flame oscillation in conical premixed flames near and far from blow-off conditions (Biswas et al. 2013). Morales et al. investigated the flame structure and the local strain rate based on CPIV during the blow-off event of a bluff-body stabilized flame (Morales et al. 2020). Chaparro et al. obtained the instantaneous flame front under the blow-off conditions in conical bluff-body stabilized premixed flames by CPIV (Chaparro and Cetegen 2006). However, there is still a lack of intensive investigation to evaluate the reliability of the CPIV, and it is necessary to explore the theoretical mechanisms and the error source for the biased performance of the CPIV under conditions close to the LBO limit, which will supply critical guidance for researchers to utilize the CPIV in the favorable combustion conditions.

Therefore, our work studied the applicability of the CPIV method under different equivalence ratios until approaching LBO. The experiments were conducted in a turbulent premixed dimethyl ether (DME)/air 2D bluff-body stabilized flame. DME is considered a cheap fuel that can be synthesized from natural gas, coal, or biofuels. In addition, DME is clean-burning and has less soot emission since it involves a high oxygen content and no C–C bond (Glaude et al. 2011). OH-PLIF, used as reference results, was conducted simultaneously with Mie-scattering since OH-PLIF is commonly adopted as an excellent method to extract the flame fronts. Furthermore, the instantaneous images and the statistical results of the mean progress variable $\langle c \rangle$, length of the flame front (L), flame surface density, stretch rate, and curvature calculated from OH-PLIF and CPIV were compared to analyze the performance of the CPIV method. The detailed experimental configuration and the data processing procedure are explained in Sect. 2. The results based on the OH-PLIF and CPIV are discussed in Sect. 3. Finally, there is a summary of this work in Sect. 4.

2 Experimental arrangements

2.1 Burner assembly

The sketch of the burner with a 2D bluff body is shown in Fig. 1. From the bottom to the top, the overall length of the test rig is 1135 mm, consisting of a cylindrical chamber (50 mm in diameter), a square flow channel, a square duct with optical accesses, and a final-stage square duct guiding the exhaust gas. The cross section of the last three square ducts is 50 mm × 50 mm. The DME/air mixture enters the burner at the bottom of the cylindrical chamber. A 20 mm-long foam metal is filled in the square flow channel, located 480 mm upstream of the 2D bluff body, to enhance the air–fuel mixing. The spark ignitor is installed about 60 mm upstream of the 2D bluff body.

Optical accesses are opened on each side of the square duct and equipped with a quartz window, as plotted in Fig. 1. The two opposite optical windows for laser
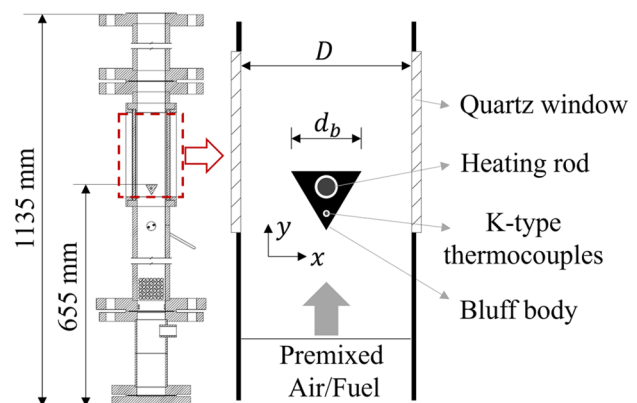

Fig. 1 Sketch of the burner with a 2D bluff body

passage are in the dimension of 148 mm (length) $\times$ 29 mm (width) $\times$ 8 mm (thickness). The other two opposite quartz glasses with a larger dimension of 148 mm (length) $\times$ 48 mm (width) $\times$ 8 mm (thickness) are designed for imaging.

The 2D bluff body used in this work is solid and fixed on one imaging quartz window by bolts. It is 49 mm long along the longitudinal direction, and its cross section is an equilateral triangle with sides of 20 mm (d_b). In order to exclude the influence of bluff-body temperature on the flame structure, a heating rod and a K-type thermocouple were pre-embedded in the 2D bluff body. A bluff-body temperature of 573 ± 10 K was monitored by a thermocouple and maintained by controlling the voltage applied to the heating rod. And the procedure was auto-controlled by the LabVIEW program.

2.2 Experimental conditions

The LBO limits were determined by keeping the air-flow constant and gradually reducing the DME flow rate by 1% each step until the blow-off occurred, and there was a waiting time of 10 s after each reduction to stabilize the flow rate. The equivalence ratio when the blow-off happened was averaged based on five repeats of this procedure, and it is 0.63 at the mixture flow rate of 7 m/s. As listed in Table 1, the flames with four different equivalence ratios ($\Phi = 0.8$ (case A1), 0.75 (case A2), 0.7 (case A3), and 0.65 (case A4)) at this flow velocity were tested and compared. The air and fuel flow rates were controlled by two mass flow controllers (Sevenstar, D07-60B series and D07-9E series), respectively.

2.3 Imaging system

The imaging system used for simultaneous OH-PLIF and Mie-scattering measurements is shown in Fig. 2.

For the OH-PLIF imaging, a tunable dye laser (Sirah Lasertechnik, Cobra-Stretch) was operated at 10 Hz, and the working medium was Rhodamine-6G dissolved in pure ethanol. The dye laser was pumped by a 532 nm Nd:YAG laser (Quantel, Q-smart 850), and the output wavelength was turned to around 283 nm to excite the Q1(6) line in the $A^1\Sigma - X^2\Pi$ ($v' = 1$, $v'' = 0$) band of the OH radical. The energy of the dye laser was about 18 mJ/pulse. A few cylindrical lenses were used to reshape the laser beam into a thin sheet of 100 mm in height. A high-speed CMOS camera (Phantom, v2012), coupled with a two-stage
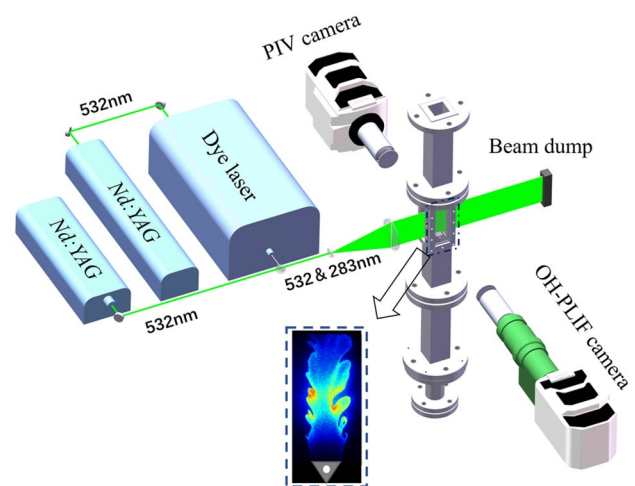

Fig. 2 The top view of the optical setup combined with the OH-PLIF and Mie-scattering measurements

image intensifier (Lambert, HiCATT) gated at 0.5 µs, was placed perpendicular to the laser sheet to capture the OH-PLIF images. A UV lens (Sodern CERCO, 105 mm f/2.8) equipped with a band-pass filter (Edmund-34980) was employed in front of the intensifier to remove interferences from other wavelengths. Due to the inhomogeneous spatial distribution of the laser energy, a cuvette in size of 120 mm $\times$ 15 mm $\times$ 10 mm (height $\times$ width $\times$ depth) was filled with ethanol and placed on top of the 2D bluff body inside the burner. The ethanol fluorescence, shown in Appendix A, can reflect the spatial intensity distribution of the laser sheet. The 1000 frames of ethanol PLIF were averaged and used to correct the OH-PLIF images.

For the Mie-scattering measurements, a 532-nm double cavity Q-switched Nd:YAG laser (Beamtech, Vlite-200) ran at 10 Hz, and the interval between the two pulses was fixed at 30 µs. The change of the flow field during this time slot can be neglected, considering the incoming velocity is 7 m/s in this work. The energy of each pulse was about 8 mJ/pulse. Similarly, the laser beam was also formed into a thin sheet of 125 mm in height. The aluminum oxide (Al_2O_3) particles with a nominal diameter of ~1.0 µm, acting as the scattering sources, were seeded into the DME/air mixture. An identical high-speed CMOS camera, running in double frame mode, was positioned perpendicular to the laser sheet to record the Mie-scattering images. A camera lens (f/8) identical to the one used for OH-PLIF and a band-pass filter (Edmund-65216) were adopted in front of the camera lens to reduce the natural luminosity of the flame.

The laser sheets for OH-PLIF and Mie-scattering overlapped spatially and longitudinally crossed the 2D bluff body. The calculated spatial resolution is 123.8 µm/pixel for OH-PLIF and 120.8 µm/pixel for Mie-scattering,

Table 1 Properties of the experimental conditions. v is the mean square root of the axial velocity, ϕ is the equivalence ratio

Case	v (m/s)	ϕ
A1	7	0.8
A2	7	0.75
A3	7	0.7
A4	7	0.65

respectively. The resolutions of the two methods are very close, indicating the resolution difference will not become an error source for comparing the images obtained by these two methods.

A master clock (PCIe 6738) was used to synchronize the timing/triggering of the cameras and lasers for simultaneous measurements of PLIF and Mie-scattering. The timing of the 283 nm laser pulse was located between the two pulses of 532 nm, implying the existence of a 15 μs delay between the OH-PLIF image and the first one of the Mie-scattering image pair. During this time delay, a max shift of 0.3 mm of the flame front was found, showing a trivial influence on the conclusion. Thus, it still can be considered a simultaneous measurement of PLIF and Mie-scattering. The 1000 images/image pairs of both methods were recorded for the data analysis.

2.4 Image processing

The two consecutive Mie-scattering images can be utilized to demonstrate the evolution of the velocity fields, and the unburnt and burnt zone can be distinguished according to the particle density gradient from each Mie-scattering image. The image calibration and velocity calculation relied on the software of DaVis 8.4. The sequential interrogation windows were decreased from 48 pixel × 48 pixel to 24 pixel × 24 pixel with an overlap of 50% by the multi-pass mode. The flame front extracted by OH-PLIF and CPIV methods is based on the scikit-image algorithms of Python, and the detailed procedure will be explained below.

For the OH-PLIF image processing, the raw image shown in Fig. 3a was firstly corrected line-by-line according to the fluorescence image of ethanol, which is explained in Appendix A, and then is displayed in Fig. 3b. $x = 0$ mm is the symmetric axis of the bluff body. Next, a 13×13 Gaussian filter was applied over the whole image for noise reduction. Gaussian filtering is widely applied to reduce the noise in the image post-processing procedure. In this work, the purpose of applying Gaussian filtering is to help improve the binarization quality during the extraction of flame fronts. Then, Otsu's thresholding method was adopted for binarization to distinguish the burnt and unburnt areas. Since there was a significant difference in the PLIF intensity distribution, the boundary extraction will bias to the wrong position if an identical threshold for binarization was employed on the whole image. Thus, the OH-PLIF image was divided along the y-axis into small regions, each with 10-pixel lines, and was binarized separately based on the intensity of each segment. And then, all these processed segments were interlinked into one binarized OH-PLIF image, as shown in Fig. 3c. It should be pointed out that the SNR of the instantaneous OH-PLIF image close to the bluff body (in the region of $y < 15$ mm) was extremely low. A significant error occurred during the flame front extraction, leading to
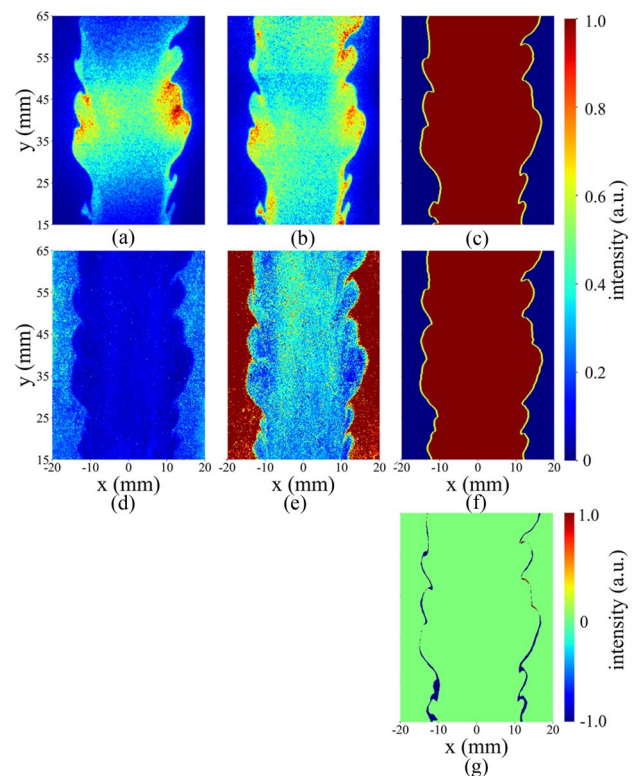

Fig. 3 Flame front extracted based on the OH-PLIF (top row) and CPIV (middle row) for case A2 with the step of **a** and **d** the raw image, **b** and **e** intensity-corrected image, **c** and **f** binarized image with emphasized contours, and **g** similarity image

distortion in calculating the mean progress variable and the flame front length. Therefore, this region was not considered in the flame front extraction.

For the CPIV image processing, the background noise was first taken in the case without particles seeded into the flow and was subtracted from the raw Mie-scattering image shown in Fig. 3d. In order to exclude the interference of local peak pixel intensity to binarization, the pixel intensities of the whole image were ranked from the minimum to the maximum, and the 80th percentile of the ascending array was defined as the threshold, and the selection criterion will be explained in detail in Appendix B. The pixel's intensity that exceeds the threshold will be assigned this threshold value, and the processed image is shown in Fig. 3e. Next, a 13×13 Gaussian filter is also utilized for noise reduction. And then, the binarization method identical to that used for the OH-PLIF image processing was applied, and the final binarized image is shown in Fig. 3f.

The flame front acquired based on OH-PLIF and CPIV was emphasized by a yellow profile in Fig. 3c and f, respectively. For both methods, the recognized burnt region is marked in red, and each pixel in this region is given an intensity of 1. In contrast, the unburnt region is denoted

in blue with the pixel intensity of 0. In order to compare the contours obtained using these two methods, the pixel intensity of Fig. 3f (the binarized Mie-scattering image) was subtracted from that of Fig. 3c (the binarized OH-PLIF image). Then, the so-called similarity image was obtained and is shown in Fig. 3g. The green background with a pixel intensity of 0 denotes that the corresponding region acquired by both methods is consistent. The blue area represents the burnt region recognized by CPIV but the unburnt region defined by OH-PLIF. On the contrary, the red area indicates the burnt region identified by OH-PLIF, but it is the unburnt part specified by CPIV. It has to be pointed out that most of the possible error sources, including the laser intensity, image resolution, optical alignments, and so on, have already been carefully considered in this work to minimize the interference from the experimental side to the similarity images.

It should be pointed out that the precision of the CPIV method is subject to the imaging of particles, which can disrupt the extraction accuracy due to their intermittent distribution and tendency to occupy multiple pixels in the Mie-scattering image. In contrast, OH-PLIF relies on the continuous distribution of OH radicals, resulting in superior spatial resolution characteristics. Consequently, a cut-off scale exists beyond which the CPIV and OH-PLIF methods may not yield consistent results. However, this discrepancy is attributed to the inherent characteristics of the two methods and is considered a systematic experimental error, which is not apparent in our work.

3 Results and discussion

3.1 Instantaneous OH-PLIF and CPIV results

Four corrected typical instantaneous OH-PLIF images at different equivalence ratios are displayed in Fig. 4a–d, and the
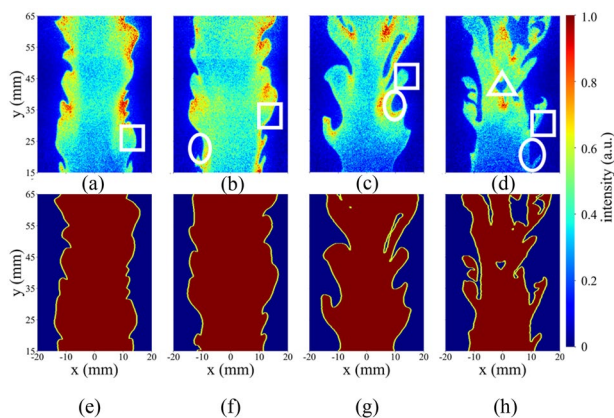
corresponding binarized images are presented in Fig. 4e–h. It can be realized that as the equivalence ratio decreases from 0.8 (Fig. 4a) to 0.65 (Fig. 4d), the burnt area gradually goes down, the wrinkling of the contour enhances, and more flame fragmentation appears, indicating the flame stability deteriorates (Chowdhury and Cetegen 2017).

Correspondingly, Fig. 5a–d compares the simultaneous corrected Mie-scattering images. The relevant binarized images are presented in Fig. 5e–h. The rough contours extracted by CPIV are similar to the results obtained by OH-PLIF shown in Fig. 4e–h. However, some delicate local structures, such as the details emphasized by the elliptical and triangular markers in Figs. 4 and 5, cannot be recognized by the CPIV method. This phenomenon occurs more frequently in cases with lower equivalence ratios, especially under the conditions approaching the LBO.

In order to compare the contours obtained using these two methods, the similarity images are considered and shown in Fig. 6. It is evident that the blue area is more prevailing than that marked in red for all tested cases with different equivalence ratios, implying that compared with the OH-PLIF method, the boundary obtained by the CPIV method is generally biased to the unburnt region. The red region, which is
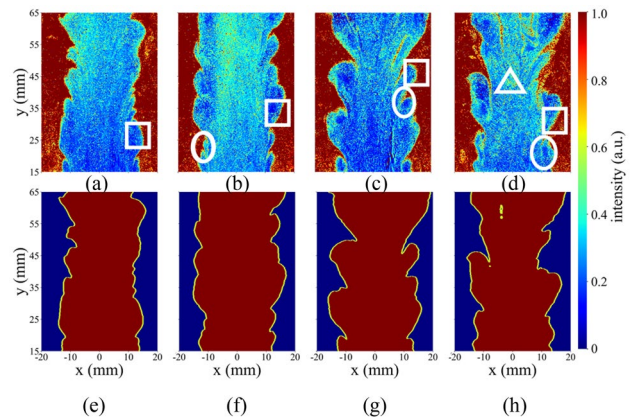

Fig. 5 **a–d** The intensity-corrected Mie-scattering images and **e–h** the binarized Mie-scattering at various equivalence ratios Φ of **a** and **e** 0.8, **b** and **f** 0.75, **c** and **g** 0.7, **d** and **h** 0.65

Fig. 4 **a–d** The intensity-corrected OH-PLIF images and **e–h** the binarized OH-PLIF at various equivalence ratios Φ of **a** and **e** 0.8, **b** and **f** 0.75, **c** and **g** 0.7, **d** and **h** 0.65
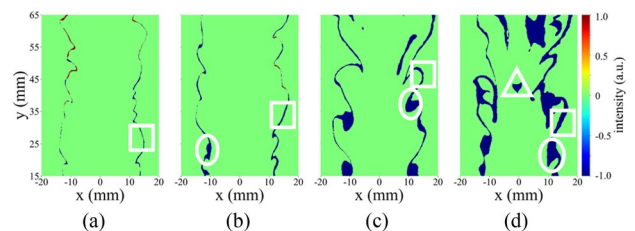

Fig. 6 The similarity images at various equivalence ratios Φ of **a** 0.8, **b** 0.75, **c** 0.7, **d** 0.65

possibly related to the 15 μs delay between the laser shot of 532 nm and 283 nm, is insignificant and can be neglected. It can be seen from Fig. 6 that in cases of stable combustion, the blue area is slender, which means that the flame fronts extracted by CPIV and OH-PLIF agree well. But the blue area increases dramatically when the equivalence ratio is decreased, indicating that the deviation between the flame fronts obtained by OH-PLIF and CPIV is more significant, particularly under the conditions approaching LBO.

The change in gas temperature due to chemical reactions will induce the gradient of local particle density. The CPIV results are directly related to the particle density. Compared to the CPIV, the OH-PLIF signal is related to the concentration of OH radical, which appears in the burnt region with high temperature and low particle density. The local temperature required to induce low particle density in CPIV is lower than that for the appearance of OH radicals. There are two primary sources of the deviation between the CPIV and OH-PLIF methods. Firstly, the flame structure has to be considered. The temperature in the preheat zone may already be high enough to result in a low particle density, and the corresponding area was defined by CPIV as a high-temperature area. As the equivalence ratio decreases, the thickness of the preheat zone in the flame increases. Thus, the deviation is more significant as the equivalence ratio decreases, emphasized by the rectangular markers in Fig. 6, which will be further discussed in Sect. 3.3. Secondly, the deviation can be attributed to aerodynamics. Instantaneous flame fronts of case A2 ($\Phi = 0.75$) extracted by OH-PLIF are displayed in Fig. 7a and marked in black. The flame fronts are overlaid with the velocity distribution, and the vectors of the velocity field are colored according to the amplitude of the normalized absolute velocity. In addition, the boundary of regions where $v_y < 0$ m/s is enclosed by a gray profile. The normalized vorticity was acquired based on the velocity

distribution and is shown in Fig. 7b, superimposed with the identical flame fronts profile in Fig. 7a. The bulk blue area in Fig. 6b, highlighted by the white ellipse, appears in the shear layer and is enclosed by a red ellipse in Fig. 7. This indicates that the unburnt gas is entrained into the concave-wrinkled regions of the OH-PLIF as a consequence of the rollup of the shear layer. The unburnt gas is encompassed by a longer flame front, which enhances the heat transfer from the reaction layer to the unburnt gas leading to a local reduction in particle density. As the equivalence ratio decreases, the interaction between the shear layer and flame is intensified, resulting in a more pronounced bias. Furthermore, the accumulation of CH_2O in concave-wrinkled regions of the OH-PLIF has been extensively documented in previous studies (Fugger et al. 2019a, b; Kariuki et al. 2015), indicating that the gas in this location has been preheated. Consequently, both reasons above contribute to the deviation between the CPIV and OH-PLIF methods depicted in Fig. 6.

Moreover, it has to be pointed out that a threshold of the particle density contrast is necessary for extracting the contours with CPIV. For example, the pocket that appears in the OH-PLIF image (marked by the triangle in Fig. 4d) but does not exist in the corresponding Mie-scattering image (Fig. 5d), is probably a pocket of the unburnt mixture in the hot burnt region downstream the bluff body. But the particle density, neither inside nor outside the pocket, is too low to build an apparent density contrast for contour extraction, contributing to the significant bias in Fig. 6d when applying the CPIV method.

The applicability of CPIV under various equivalence ratios discussed above shows that although the result of the CPIV method agrees well with that of OH-PLIF in cases of stable combustion, the accuracy of CPIV gets worse as the equivalence ratio decreases.

3.2 Statistical OH-PLIF and CPIV results

The results above are based on the instantaneous image, and the statistical results will be discussed in this section. In the following discussion, cases A2 ($\Phi = 0.75$) and A4 ($\Phi = 0.65$) are analyzed quantitatively since these two cases are representative of the stable and near-LBO conditions. The 100 binarized OH-PLIF and CPIV images and the extracted contours for cases A2 and A4 are overlaid and shown in Figs. 8 and 9, respectively. A detailed analysis of the impact of the number of snapshots on statistical results has been included in Appendix C. For both Figs. 8 and 9, the top row is obtained from OH-PLIF, and the bottom row is calculated by CPIV.

Many combustion models based on the flamelet paradigm employ a progress variable (Peters 2000), which can be used to estimate the flame surface intensity and the brush thickness. In this study, the mean progress variable $\langle c \rangle$ is
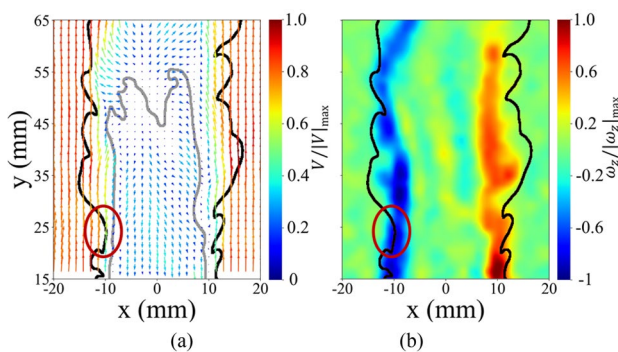

Fig. 7 Instantaneous image of case A2, representing **a** the flame fronts (marked by black lines) overlaid on the normalized velocity vectors and the boundary of regions where $v_y < 0$ m/s (marked by gray lines), and **b** the normalized vorticity distribution superimposed by the identical flame front contour (black lines)
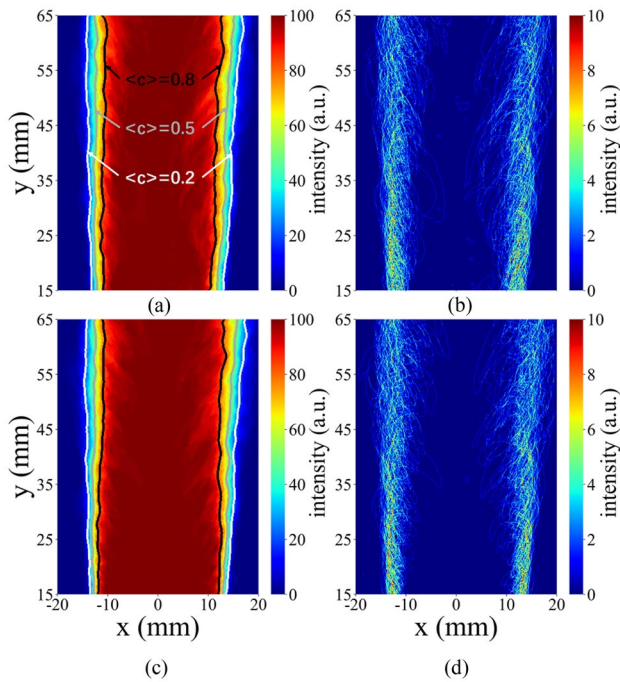
Fig. 8 The overlaid 100 images for case A2 of **a** the binarized OH-PLIF image, **b** flame front contours extracted based on OH-PLIF, **c** the binarized Mie-scattering image, and **d** flame front contours extracted based on CPIV. The mean progress variable contours of $\langle c \rangle = 0.2$ (white), 0.5 (gray), and 0.8 (black) are displayed in (**a**) and (**c**)

Fig. 9 The overlaid 100 images for case A4 of **a** the binarized OH-PLIF image, **b** flame front contours extracted based on OH-PLIF, **c** the binarized Mie-scattering image, and **d** flame front contours extracted based on CPIV. The mean progress variable contours of $\langle c \rangle = 0.2$ (white), 0.5 (gray), and 0.8 (black) are displayed in (**a**) and (**c**)

calculated by the following expression (Kobayashi et al. 2005):

$$\langle c \rangle = \sum_{n=1}^{N} c_n(x, y)/N \tag{1}$$

where $c_n(x, y)$ is the pixel intensity ($c_n = 0$ within fresh reactants and $c_n = 1$ within burnt products) at the point (x, y) of the nth instantaneous binarized image, and N is the number of images for averaging. The mean progress variable contour of $\langle c \rangle = 0.5$ is usually deemed as the mean location of the flame front (Driscoll 2008). The contours of $\langle c \rangle = 0.2$, 0.5, and 0.8 are overlaid with the binarized images in Fig. 8 and 9 and represented in white, gray, and black curves. It can be seen from Fig. 8 that for case A2, both the binarized images and contours extracted using the two methods are in good agreement. However, the deviation between the results obtained by the two methods for case A4 is apparent in Fig. 9, especially in the region of $y > 35$ mm.

The position of the same $\langle c \rangle$ of the left branch at the downstream position of $y = 40$ mm in Figs. 8 and 9 is compared in Fig. 10. The results based on CPIV and OH-PLIF are denoted by dashed and solid lines, and cases A2 and A4 are marked in black and red, respectively. The curve of case A2 obtained based on the OH-PLIF method departs from
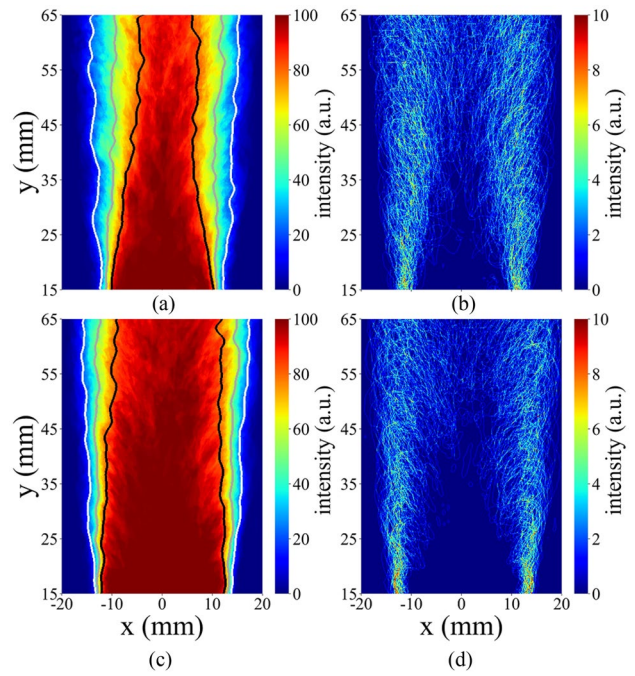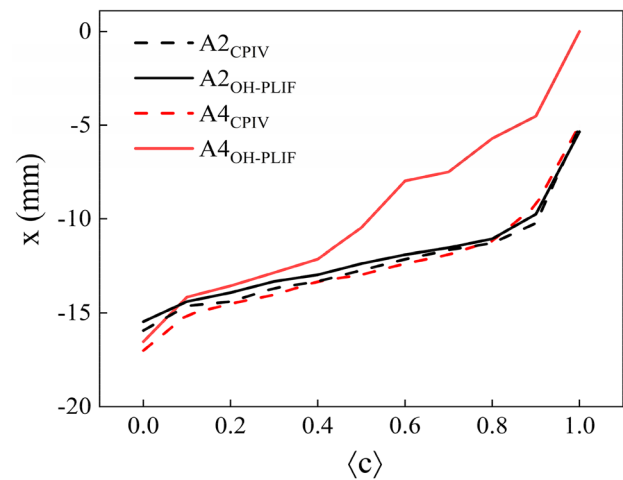

Fig. 10 The x-locations based on OH-PLIF and CPIV as a function of the mean progress variable $\langle c \rangle$ at the downstream position of $y = 40$ mm for cases A2 and A4. $\langle c \rangle = 0$ is on the outer side of the flame, and $\langle c \rangle = 1$ is close to the flame center

case A4, indicating the excellent capability of OH-PLIF to recognize the stable case and the one approaching LBO. The x-location of larger $\langle c \rangle$ is getting closer to the symmetric axis for both cases, and the one of case A4 is closer to the

$x = 0$ compared to that of case A2. It demonstrates that the flame shrinks along the x-axis, and the separation between the two branches of the flame fronts becomes narrower when lowering the equivalence ratio, which is consistent with the findings in Figs. 8a and 9a. For case A2, the two curves obtained by OH-PLIF and CPIV are very close, indicating that the flame fronts extracted by the two methods show good agreement. In contrast, for case A4, the line based on CPIV shows up at a much larger absolute value of x-location than that obtained by OH-PLIF, indicating that CPIV recognizes more area as the burnt region.

In order to quantitatively evaluate the difference between the lines obtained by the two methods in Fig. 10, the difference (S) of the distance between the position of the identical $\langle c \rangle$ along the x-axis is estimated by the equation below:

$$S = \left[\sum_{\langle c \rangle = 0}^{1} \left(\left| x_{\text{CPIV}, \langle c \rangle} - x_{\text{OH-PLIF}, \langle c \rangle} \right| \right) \right] / n \tag{2}$$

where $x_{\text{CPIV}, \langle c \rangle}$ and $x_{\text{OH-PLIF}, \langle c \rangle}$ were obtained based on CPIV and OH-PLIF, respectively. n is the number of $\langle c \rangle$ in Fig. 10. S of case A2 is 0.32 mm, which implies that the flame fronts extracted by CPIV and OH-PLIF agree very well, and the CPIV is reliable under stable combustion conditions. In contrast, for the unstable case approaching LBO, S is 2.84 mm in case A4, which is 8.9 times the value of case A2, demonstrating a noticeable discrepancy between the contours obtained based on the two methods. Furthermore, the bias is negligible when $\langle c \rangle$ is below 0.4, indicating that the interaction between the shear layer and flame is stronger in the spatial location between $\langle c \rangle = 0.4$ and 1 of unstable flames.

Another parameter d_c is the separation along the x-direction between the left branch of $\langle c \rangle = 0.5$ acquired by CPIV and OH-PLIF, marked by the gray lines shown in Fig. 8 and 9, respectively. The values of d_c at different downstream distances along the y-axis are estimated and shown in Fig. 11. A smaller value of d_c indicates a better agreement between the CPIV and OH-PLIF. It can be noticed that for case A2, d_c drops slightly as the downstream distance increases, probably due to the intensified shear layer-flame interaction near the bluff body. While in case A4, the trend of d_c is opposite to that of case A2, and d_c increases for longer downstream distances. The lower d_c in the upstream is related to the hot RZ. The high-temperature gas in the RZ helps to stabilize the flame, which is called "back-support" (Skiba et al. 2018). It can be found that the mean value of d_c in case A4 (2.92 mm) is 9.4 times that in the case of A2 (0.31 mm). Compared with the results of $\langle c \rangle = 0.5$ obtained by the OH-PLIF method, there is a significant spatial bias when extracting the flame fronts based on CPIV under near-LBO conditions (case A4).

Furthermore, the flame front wrinkling is critical in analyzing the turbulent flame speed (Driscoll 2008). In this study, the wrinkling of the flame front is quantized by the
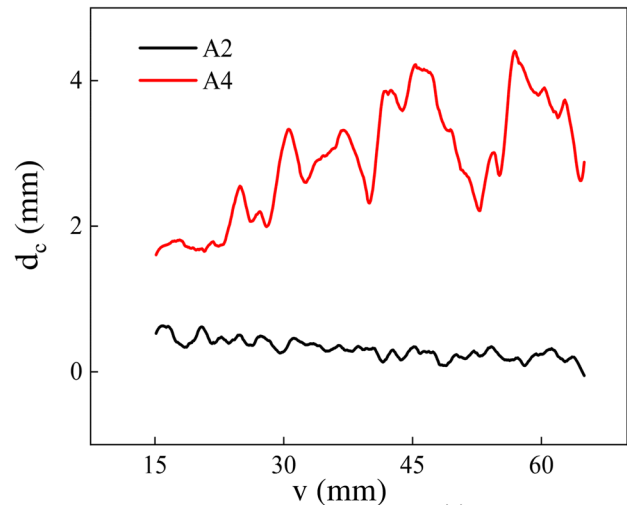

Fig. 11 The difference between the left branch of $\langle c \rangle = 0.5$ profile obtained by CPIV and OH-PLIF as a function of downstream distance for cases A2 and A4

length of the flame front (L), which is calculated by the following expression:

$$L = \frac{1}{q} \sum_{x=1}^{M/2} I(x, y) \tag{3}$$

where q is the correction factor and equals 8.4 pixel/mm obtained from the image calibration process between the image and object domain, and M is the pixel column number of each image. $I(x, y)$ is the pixel intensity of location (x, y) in Figs. 8b, d and 9b, d. The calculated L based on the left half image as a function of downstream distance is plotted in Fig. 12. L obtained by OH-PLIF was considered the reference value, and the bias of CPIV was evaluated. The dashed line represents the result obtained by CPIV, and the solid line displays the result acquired from OH-PLIF. It can be seen that the values of dashed lines are always smaller than the solid lines for both cases A2 (black) and A4 (red), and the reduced amount of mean value of L for case A4 is 22.7%, which is 2.9 times that value of case A2 (7.7%). In the downstream area of $y > 35$ mm, the calculated L values using the OH-PLIF method for case A4 are obviously greater than that based on the CPIV method because the CPIV cannot recognize the delicate structures along the flame front for unstable combustion case, such as the structures marked by ellipse and triangle in Fig. 6.

In this section, some physical quantities based on the flame front statistics, such as flame surface density, stretch rate, and curvature, have also been evaluated to better understand the flame structure and dynamics.

The 2D flame surface density (FSD, denoted as Σ), which is the ratio of the local flame front length to the flame area, is
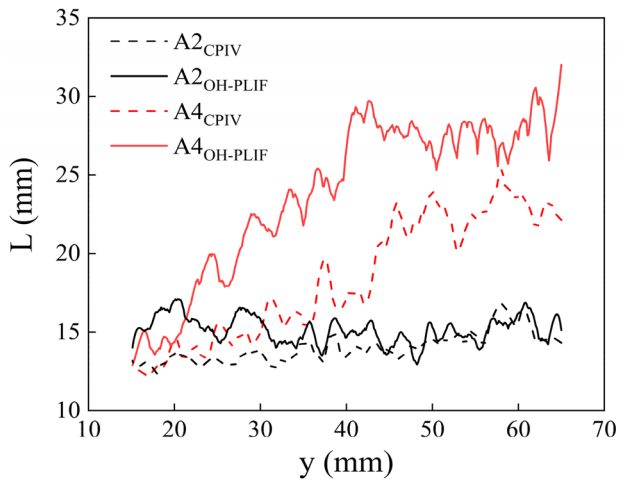
Fig. 12 The length of the left branch of the flame fronts (L) as a function of downstream distance obtained by OH-PLIF and CPIV for cases A2 and A4

an important parameter to describe the relationship between the turbulent flame speed and the structure of the flame front (Chowdhury and Cetegen 2017). The FSD can be calculated based on the flame brush (Zhang et al. 2014) (as shown in Figs. 8b, d and 9b, d). In this work, an interrogation window of 5×5 pixels is adopted, and it has been demonstrated that the Σ is hardly influenced by the size of Δx (Filatyev et al. 2005). At the downstream position of $y = 40$ mm, Σ distributions for cases A2 and A4 calculated from the OH-PLIF and CPIV methods are displayed in Fig. 13. It demonstrates that Σ obtained by the two methods is in a good agreement under case A2. However, in case A4, there is a notable discrepancy in Σ obtained using CPIV compared with OH-PLIF, and the bias is primarily toward the unburnt region. This
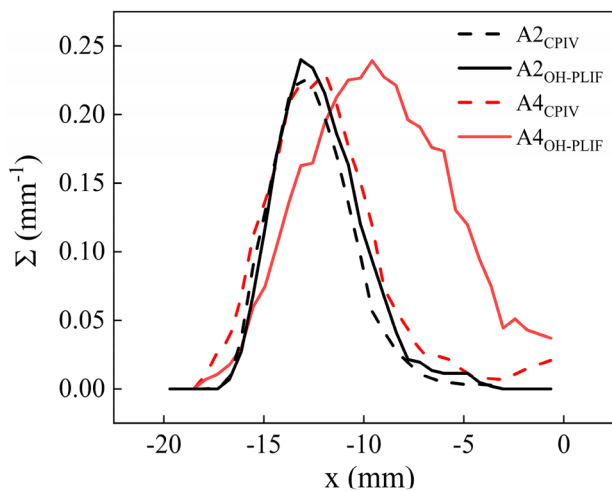
observation is consistent with the instantaneous results presented in Fig. 6. It is noteworthy that the maximum values of Σ obtained by both methods are similar. Nevertheless, the range of Σ distribution extracted based on CPIV is considerably narrower than that obtained by OH-PLIF. This difference is mainly attributed to the L extracted by CPIV is shorter than that obtained by OH-PLIF, as illustrated in Fig. 12.

The stretch rate (κ_s) of the flame front is widely used to enhance the understanding of flame dynamics. In this study, the stretch rate was calculated from 100 images using CPIV and OH-PLIF under two cases, A2 and A4. The calculation method is consistent with Ref. (Tuttle et al. 2012). The probability density functions of the stretch rate are shown in Fig. 14. The results demonstrate that the stretch rate values obtained using the CPIV are lower than those obtained by the OH-PLIF for both cases. Specifically, for case A2, the difference between the stretch rates obtained using the two methods is small, while for case A4, the stretch rate obtained using the CPIV method is significantly lower than that obtained using the OH-PLIF. Combined with Fig. 6, this difference is attributed to the bias of the flame front position obtained using the CPIV toward the unburnt region, resulting in a lower stretch rate than at the actual flame front. These findings suggest that under the near-LBO condition the stretch rate of the flame front calculated using the CPIV method is significantly lower than the actual results. This should be taken into account by researchers in future studies.

Finally, the curvature of the flame front obtained by CPIV and OH-PLIF methods under two cases, A2 and A4, was calculated and compared using the method described in Ref. (Chowdhury and Cetegen 2017). The results presented in Fig. 15 reveal that the distribution obtained by the CPIV method is slightly wider for case A2, which is consistent
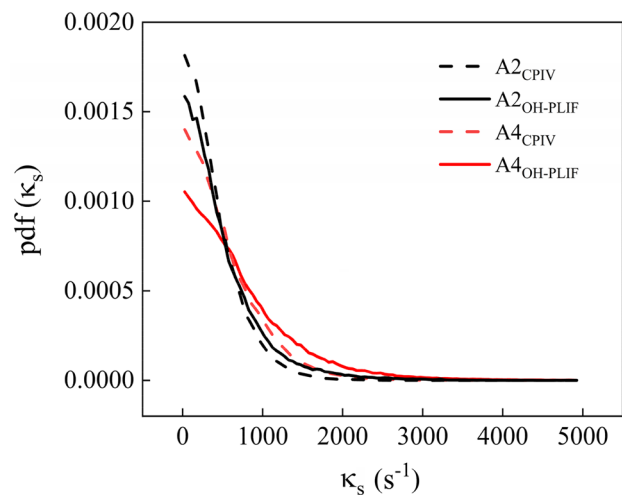

Fig. 13 Flame surface density distributions using CPIV and OH-PLIF for cases A2 and A4

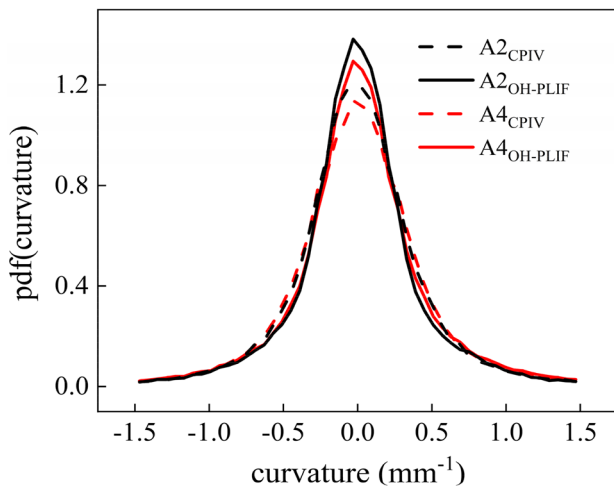**Fig. 14** Probability density functions of $|\kappa_s|$ using CPIV and OH-PLIF for cases A2 and A4

Fig. 15 Probability density functions of curvature using CPIV and OH-PLIF for cases A2 and A4

with the findings in Ref. (Pfadler et al. 2007) and may be attributed to the more noise of the images. Interestingly, the curvature obtained by both methods is very similar for case A4. This suggests that the probability density functions of curvature obtained by the CPIV method may have a certain degree of credibility, as some flame fronts exhibit high similarity even when the flame front position differs significantly.

3.3 The theoretical mechanisms for the deviation between the two methods

The mean value of d_c and the mean reduction rate of L are defined as d_m and L_r, respectively. The corresponding values of four cases are calculated to evaluate the performance of the CPIV method at various equivalence ratios. It can be realized in Fig. 16 that both d_m and L_r go up as the equivalence ratio decreases, indicating that the CPIV
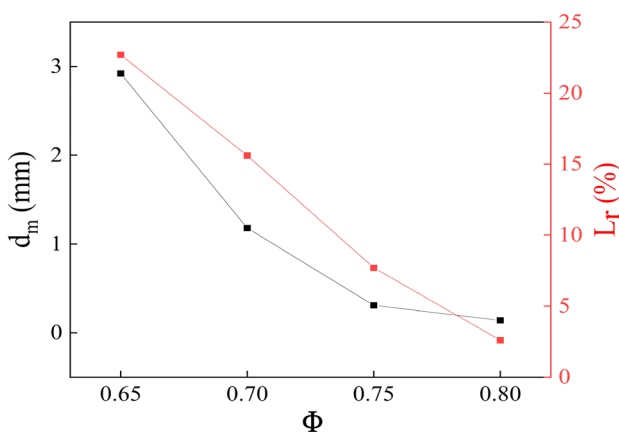
method suffers a higher bias under unstable conditions. As the equivalence ratio goes down, the wrinkling of the flame front enhances, more flame fragmentation appears, and the L_r rises obviously. The results of Fig. 16 demonstrate that the CPIV method can accurately extract the flame front for stable flames, consistent with prior reports (Pfadler et al. 2007). However, for the unsteady flames approaching LBO, significant errors are observed in the extracted flame front using the CPIV, as far as we know, which were not reported before.

In addition, the nonlinear behavior of d_m is evident and related to the structure of premixed flame. The chemical structure of the laminar premixed flame was obtained using the PREMIX tool combined with the mechanism from Zhao et al. (2008). Typical profiles of the normalized mole fraction of OH and CH_2O and the inverse temperature are shown in Fig. 17. The extraction of the flame front based on the CPIV is directly related to the density gradient and is determined by the maximum gradient of the inverse temperature, which is marked by a blue dashed line in Fig. 17. According to the experimental results in Ref. (Pfadler et al. 2007), the flame front contour extracted by OH-PLIF can be used to estimate the location of the most intensive heat release. In another way, the maximum heat release can be calculated by multiplying the concentration of CH_2O and OH, and its location is denoted by the orange line in Fig. 17. It is evident that there is a gap between the maximum gradient of inverse temperature (blue dashed line at 0.51 mm) and the OH-PLIF contour (orange line at 0.95 mm), which is a possible reason for the bias in the extraction of the flame front using CPIV and OH-PLIF.

A parameter of spatial distances (δ) is defined as the separation between the maximum gradient of inverse temperature (blue dashed line in Fig. 17) and the OH-PLIF contour (orange dashed line in Fig. 17). The value of δ
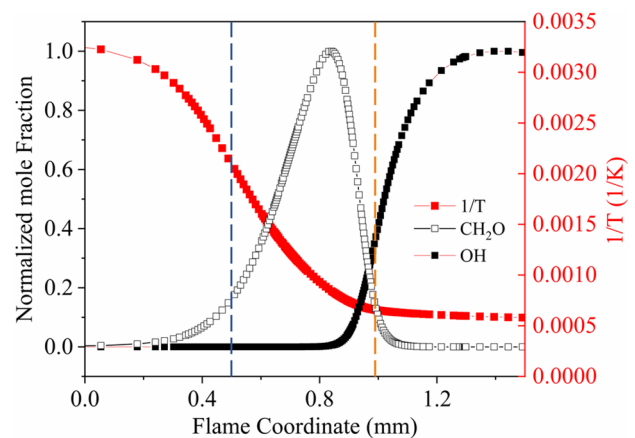

Fig. 16 The mean distance d_m and reduction rate L_r at various equivalence ratios

Fig. 17 The normalized mole fraction of OH and CH_2O and the inverse temperature in the premixed DME/air flame ($\Phi = 0.65$)

under different equivalence radios was estimated and is shown in Fig. 18. The value of δ increases nonlinearly when reducing the equivalence ratio. In addition, as a marker of the preheat zone in hydrocarbon fuels, the CH_2O radical is distributed in the region between the drop of inverse temperature and the rise of the OH mole fraction, as shown in Fig. 17. The full width of half maximum (FWHM) of the CH_2O layer thickness is calculated as a function of the equivalence ratio and plotted in Fig. 18. It can be seen that the FWHM of the CH_2O layer thickness rises nonlinearly when decreasing the equivalence ratio. In conclusion, the deviation due to the flame structure, emphasized by the rectangular markers in Fig. 6, is highly related to the CH_2O. It should be pointed out that the above results are based on the laminar flame calculations. The Reynolds number of the test cases in this work was estimated to be around 9000, and the flame structure is consistent with that of a laminar flame. Therefore, although CH_2O distribution was not measured, the results of laminar flames calculated by CHEMKIN are valid for our test cases.

Additionally, it has been demonstrated in previous experimental investigations that the CH_2O signal is observed both in the preheat layer of flame and the concave-wrinkled location of OH-PLIF. Therefore, the deviation between the CPIV and OH-PLIF can almost be used as a potential marker of the spatial existence of CH_2O, particularly for unstable flames. The thickness of the CH_2O layer balloons as the equivalence ratio decreases for many different kinds of hydrocarbon fuels (Fugger et al. 2019a, b; Kariuki et al. 2016; Kariuki et al. 2015). Thus, the conclusion is not dependent on the type of hydrocarbon fuels. This deviation between the CPIV and OH-PLIF provides the possibility to estimate the CH_2O distribution by simultaneous O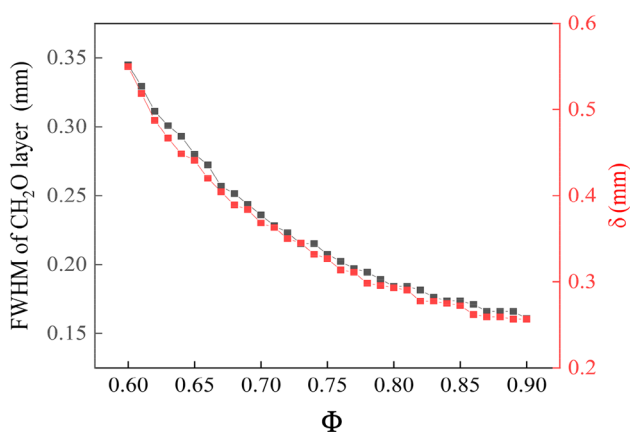H-PLIF and PIV measurement without the simultaneous application of a CH_2O-PLIF system, which is practical for experimental measurements.

4 Conclusions

The applicability of CPIV under different equivalence ratios from stable combustion to near LBO was studied in premixed 2D bluff-body flames. The OH-PLIF and CPIV were applied simultaneously to obtain the flame front, and the results were compared to evaluate the extraction accuracy of the CPIV method. It can be found that, as the equivalence ratio decreases, the deviation between the two methods expands evidently, which is severe under conditions close to LBO. For all the tested cases, the difference between the extracted flame front based on the CPIV and OH-PLIF methods is related to the flame structure and aerodynamics. For stable combustion, the flame front obtained using the two methods agrees very well, but a slight difference exists in the upstream flame, possibly caused by the intensified shear layer-flame interaction near the bluff body. However, for the flames approaching LBO with a low equivalence ratio, the deviation in the downstream area is more significant than that in the upstream region, which is related to the "back-support" of the hot RZ.

As the equivalence ratio decreases, the reduced amount of the flame front length (L_r) and the location deviation (d_m) of the mean progress variable ($\langle c \rangle = 0.5$) obtained by the two methods increase sharply. The corresponding values in case A4 are about 9 and 3 times that of case A2, respectively. The rise of L_r is related to more wrinkled contour and flame fragmentation. Recognizing them utilizing the CPIV method is challenging, especially when approaching the LBO limit. Furthermore, the flame surface density (Σ) and stretch rate (κ_s) for case A2 acquired using two methods are consistent. However, the CPIV method yielded a narrower range of Σ distribution and a lower κ_s for case A4. Notably, the curvature probability density functions obtained by the CPIV method are deemed credible for both cases despite significant location differences in the flame front found in some positions.

Based on the structure of the premixed flame and previous studies, the deviation between these two methods can be applied to represent the spatial existence of the CH_2O in the preheat layer of flame and the concave-wrinkled location of the OH-PLIF, especially in unstable combustions. This allows the possibility of simultaneously measuring the flow field, CH_2O, and OH spatial distributions in turbulent premixed flames using only PIV and OH-PLIF. It is significant to simplify the experimental setup and reduce the cost, and more investigations will be conducted to validate this point in our future work. In conclusion, the findings in this work provide valuable insights into the reliability of CPIV under

Fig. 18 δ and FWHM of CH_2O layer thickness as a function of equivalence ratio

various conditions and verify the applicability of the CPIV method under conditions close to LBO.

Appendix A

In order to reduce the influence of the spatial inhomogeneous of the laser on the OH-PLIF results, the 1000 fluorescence images of ethanol were averaged and are shown in Fig. 19a. As shown in Fig. 19b, the intensity values in Fig. 19a were summed along the x-axis and normalized by the maximum value, and the relative intensity of the laser at various y-locations was obtained and is shown in Fig. 19b. The raw OH-PLIF image was corrected line-by-line according to the relative value in Fig. 19b.

Appendix B

In order to evaluate the influence of the threshold values on the quality of the similarity images, different threshold values were tested. The similarity images were obtained and compared. Figure 20a displays the areas of the blue and red regions in the similarity images as a function of the threshold percentile. It can be seen that a flat basin exists when the threshold ranges from 65 to 95th percentile. The binarized images obtained with a 50th, 80th, and 100th percentile threshold are shown in Fig. 20b–d. A large number of areas are obviously recognized wrongly when the threshold is outside the range of the flat basin, as shown in Fig. 20b and d. Considering the intensity fluctuation between different data sets, a moderate threshold value of the 80th percentile was selected in the flame front extraction. The result in Fig. 20c shows an excellent extraction quality.
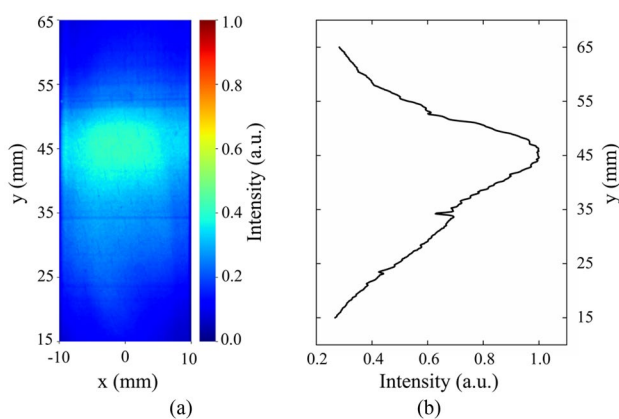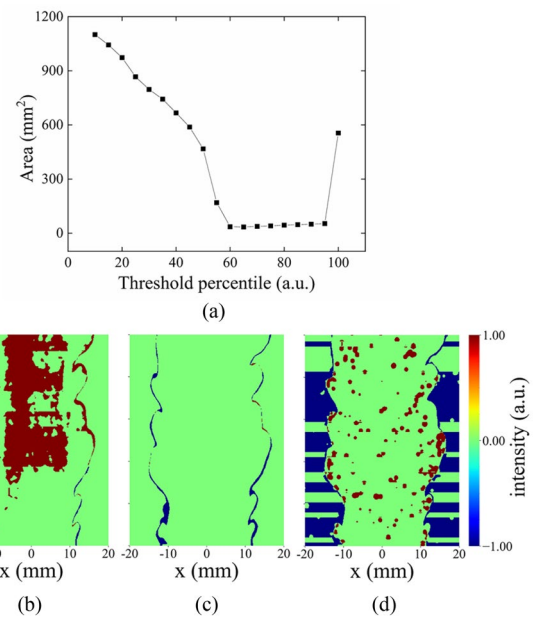

Fig. 20 a The total area of the blue and red regions in the similarity images as a function of the threshold percentile and the similarity images obtained with different thresholds of **b** 50%, **c** 80%, and **d** 100%

Appendix C

To evaluate the impact of the number of snapshots on statistical results, various numbers of snapshots (10, 50, 100, 150, and 200) were examined for case A4. And then, five corresponding overlaid binarized Mie-scattering images were generated. At the downstream position of $y = 40$ mm, the $\langle c \rangle$ values for different x positions of the left branch were calculated and are represented in Fig. 21, and the calculation approach is similar to Fig. 10. Notably, significant
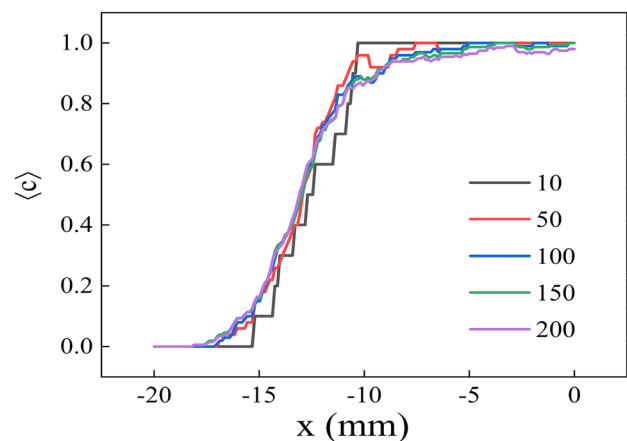

Fig. 19 a The normalized fluorescence image of ethanol and **b** the relative intensity of laser at various y-locations

Fig. 21 The $\langle c \rangle$ values for different x positions at $y = 40$ mm with different numbers of snapshots for case A4

differences were observed between the statistical results based on 10 and 50 images. However, as the number of snapshots increased to 100 or more, the $\langle c \rangle$ values for different x positions became very close, and the curves appeared smoother. Furthermore, the correlation coefficient (Rodgers and Nicewander 1988) between the $\langle c \rangle$ values calculated from 100 to 200 snapshots is 0.9997. These findings indicate that statistical significance has already been achieved with 100 snapshots.

Author contributions XW was involved in the methodology, experiments, software, investigation, writing-original draft, visualization, data curation, and writing—reviewing and editing. KL was involved in the experiments and visualization. CF contributed to the experiments and writing—reviewing and editing. JY helped with the writing—review and editing, and supervision. YG contributed to the conceptualization, methodology, writing-reviewing and editing, funding acquisition, project administration, and supervision.

Data availability Data and materials supporting the findings of this study are available on request from the corresponding author, Yi Gao.

Declarations

Conflict of interest The authors declare that they have no competing interests.

Ethical approval Not applicable.

References

Ayoolan BO, Balachandran R, Frank JH, Mastorakos E, Kaminski CF (2006) Spatially resolved heat release rate measurements in turbulent premixed flames. Combust Flame 144:1–16. https://doi.org/10.1016/j.combustflame.2005.06.005

Barlow RS, Wang GH, Anselmo-Filho P, Sweeney MS, Hochgreb S (2009) Application of Raman/Rayleigh/LIF diagnostics in turbulent stratified flames. Proc Combust Inst 32:945–953. https://doi.org/10.1016/j.proci.2008.06.070

Biswas S, Kopp-Vaughn K, Renfro MW, Cetegen BM (2013) Phase resolved characterization of conical premixed flames near and far from blowoff. Combust Flame 160:2843–2855. https://doi.org/10.1016/j.combustflame.2013.06.014

Chaparro AA, Cetegen BM (2006) Blowoff characteristics of bluff-body stabilized conical premixed flames under upstream velocity modulation. Combust Flame 144:318–335. https://doi.org/10.1016/j.combustflame.2005.08.024

Chowdhury BR, Cetegen BM (2017) Experimental study of the effects of free stream turbulence on characteristics and flame structure of bluff-body stabilized conical lean premixed flames. Combust Flame 178:311–328. https://doi.org/10.1016/j.combustflame.2016.12.019

Driscoll J (2008) Turbulent premixed combustion: Flamelet structure and its effect on turbulent burning velocities. Prog Energy Combust Sci 34:91–134. https://doi.org/10.1016/j.pecs.2007.04.002

Driscoll JF, Chen JH, Skiba AW, Carter CD, Hawkes ER, Wang H (2020) Premixed flames subjected to extreme turbulence: some questions and recent answers. Prog Energy Combust Sci. https://doi.org/10.1016/j.pecs.2019.100802

Filatyev SA, Driscoll JF, Carter CD, Donbar JM (2005) Measured properties of turbulent premixed flames for model assessment, including burning velocities, stretch rates, and surface densities. Combust Flame 141:1–21. https://doi.org/10.1016/j.combustflame.2004.07.010

Fugger CA, Roy S, Caswell AW, Rankin BA, Gord JR (2019b) Structure and dynamics of CH_2O, OH, and the velocity field of a confined bluff-body premixed flame, using simultaneous PLIF and PIV at 10 kHz. Proc Combust Inst 37:1461–1469. https://doi.org/10.1016/j.proci.2018.05.014

Fugger CA, Paxton B, Gord JR, Rankin BA, Caswell AW (2019a) Measurements and analysis of flow-flame interactions in bluff-body-stabilized turbulent premixed propane-air flames. In: AIAA scitech 2019a forum. https://doi.org/10.2514/6.2019-0733

Geikie MK, Carr ZR, Ahmed KA, Forliti DJ (2017) On the flame-generated vorticity dynamics of Bluff-body-stabilized premixed flames. Flow Turbul Combust 99:487–509. https://doi.org/10.1007/s10494-017-9822-1

Glaude PA, Fournet R, Bounaceur R, Molie`re M (2011) DME as a potential alternative fuel for gas turbines: a numerical approach to combustion and oxidation kinetics. In: ASME 2011 turbo expo: turbine technical conference and exposition, pp 649–658. https://doi.org/10.1115/GT2011-46238

Hartung G, Hult J, Kaminski CF, Rogerson JW, Swaminathan N (2008) Effect of heat release on turbulence and scalar-turbulence interaction in premixed combustion. Phys Fluids. https://doi.org/10.1063/1.2896285

Hartung G, Hult J, Balachandran R, Mackley MR, Kaminski CF (2009) Flame front tracking in turbulent lean premixed flames using stereo PIV and time-sequenced planar LIF of OH. Appl Phys B 96:843–862. https://doi.org/10.1007/s00340-009-3647-0

Hassel EP, Linow S (2000) Laser diagnostics for studies of turbulent combustion. Meas Sci Technol 11:R37–R57. https://doi.org/10.1088/0957-0233/11/2/201

Kariuki J, Dowlut A, Yuan R, Balachandran R, Mastorakos E (2015) Heat release imaging in turbulent premixed methane-air flames close to blow-off. Proc Combust Inst 35:1443–1450. https://doi.org/10.1016/j.proci.2014.05.144

Kariuki J, Dowlut A, Balachandran R, Mastorakos E (2016) Heat release imaging in turbulent premixed ethylene-air flames near blow-off. Flow Turbul Combust 96:1039–1051. https://doi.org/10.1007/s10494-016-9720-y

Knaus DA, Gouldin FC, Bingham DC (2002) Assessment of crossed-plane tomography for flamelet surface normal measurements.

Combust Sci Technol 174:101–134. https://doi.org/10.1080/713712908

Knaus D, Sattler S, Gouldin F (2005) Three-dimensional temperature gradients in premixed turbulent flamelets via crossed-plane Rayleigh imaging. Combust Flame 141:253–270. https://doi.org/10.1016/j.combustflame.2005.01.008

Kobayashi H, Seyama K, Hagiwara H, Ogami Y (2005) Burning velocity correlation of methane/air turbulent premixed flames at high pressure and high temperature. Proc Combust Inst 30:827–834. https://doi.org/10.1016/j.proci.2004.08.098

Marshall A, Lundrigan J, Venkateswaran P, Seitzman J, Lieuwen T (2017) Measurements of stretch statistics at flame leading points for high hydrogen content fuels. J Eng Gas Turbines Power-Trans Asme. https://doi.org/10.1115/1.4035819

Morales AJ, Reyes J, Joo PH, Boxx I, Ahmed KA (2020) Pressure gradient tailoring effects on the mechanisms of bluff-body flame extinction. Combust Flame 215:224–237. https://doi.org/10.1016/j.combustflame.2020.01.035

Morales AJ, Genova T Jr, Reyes J, Boxx I, Ahmed KA (2021) Turbulence-driven blowout instabilities of premixed bluff-body flames. Flow Turbul Combust. https://doi.org/10.1007/s10494-021-00269-8

Nguyen QV, Paul PH (1996) The time evolution of a vortex-flame interaction observed via planar imaging of CH and OH. Proc Combust Inst 26:357–364. https://doi.org/10.1016/S0082-0784(96)80236-0

Peters N (2000) Turbulent combustion. Cambridge University Press, Cambridge, pp 78–86

Pfadler S, Beyrau F, Leipertz A (2007) Flame front detection and characterization using conditioned particle image velocimetry (CPIV). Opt Express 15:15444–15456. https://doi.org/10.1364/oe.15.015444

Pfadler S, Leipertz A, Dinkelacker F (2008) Systematic experiments on turbulent premixed Bunsen flames including turbulent flux measurements. Combust Flame 152:616–631. https://doi.org/10.1016/j.combustflame.2007.11.006

Pfadler S, Dinkelacker F, Beyrau F, Leipertz A (2009) High resolution dual-plane stereo-PIV for validation of subgrid scale models in large-eddy simulations of turbulent premixed flames. Combust Flame 156:1552–1564. https://doi.org/10.1016/j.combustflame.2009.02.010

Ranjan R, Ebi DF, Clemens NT (2019) Role of inertial forces in flame-flow interaction during premixed swirl flame flashback. Proc Combust Inst 37:5155–5162. https://doi.org/10.1016/j.proci.2018.09.010

Rising CJ, Morales AJ, Geikie MK, Ahmed KA (2021) The effects of turbulence and pressure gradients on vorticity transport in premixed bluff-body flames. Phys Fluids. https://doi.org/10.1063/5.0031068

Rodgers L, Nicewander WA (1988) Thirteen ways to look at the correlation coefficient. Stat 42:59–66. https://doi.org/10.1080/00031305.1988.10475524

Shimura M, Ueda T, Choi G-M, Tanahashi M, Miyauchi T (2011) Simultaneous dual-plane CH PLIF, single-plane OH PLIF and dual-plane stereoscopic PIV measurements in methane-air turbulent premixed flames. Proc Combust Inst 33:775–782. https://doi.org/10.1016/j.proci.2010.05.026

Skiba AW, Wabel TM, Carter CD, Hammack SD, Temme JE, Driscoll JF (2018) Premixed flames subjected to extreme levels of turbulence part I: Flame structure and a new measured regime diagram. Combust Flame 189:407–432. https://doi.org/10.1016/j.combustflame.2017.08.016

Tanahashi M, Murakami S, Choi G-M, Fukuchi Y, Miyauchi T (2005) Simultaneous CH–OH PLIF and stereoscopic PIV measurements of turbulent premixed flames. Proc Combust Inst 30:1665–1672. https://doi.org/10.1016/j.proci.2004.08.270

Tuttle SG, Chaudhuri S, Kostka S et al (2012) Time-resolved blowoff transition measurements for two-dimensional bluff body-stabilized flames in vitiated flow. Combust Flame 159:291–305. https://doi.org/10.1016/j.combustflame.2011.06.001

Tuttle SG, Chaudhuri S, Kopp-Vaughan KM et al (2013) Lean blowoff behavior of asymmetrically-fueled bluff body-stabilized flames. Combust Flame 160:1677–1692. https://doi.org/10.1016/j.combustflame.2013.03.009

Tyagi A, O'Connor J (2020) Towards a method of estimating out-of-plane effects on measurements of turbulent flame dynamics. Combust Flame 216:206–222. https://doi.org/10.1016/j.combustflame.2020.02.010

Zhang M, Wang J, Xie Y et al (2014) Measurement on instantaneous flame front structure of turbulent premixed CH4/H2/air flames. Exp Thermal Fluid Sci 52:288–296. https://doi.org/10.1016/j.expthermflusci.2013.10.002

Zhao Z, Chaos M, Kazakov A, Dryer F (2008) Thermal decomposition reaction and a comprehensive kinetic model of dimethyl ether. Int J Chem Kinet 40:1–18. https://doi.org/10.1002/kin.20285